The Astrophysical Journal, 647:922–933, 2006 August 20

SPITZER OBSERVATIONS OF THE BRIGHTEST GALAXIES IN X-RAY-LUMINOUS CLUSTERS

E. Egami,[1] K. A. Misselt,[1] G. H. Rieke,[1] M. W. Wise,[2] G. Neugebauer,[1] J.-P. Kneib,[3,4] E. Le Floc'h,[1,5] G. P. Smith,[4,6] M. Blaylock,[1] H. Dole,[1,7] D. T. Frayer,[8] J.-S. Huang,[9] O. Krause,[1] C. Papovich,[1] P. G. Pérez-González,[1] and J. R. Rigby[1]

Received 2006 January 11; accepted 2006 March 15

ABSTRACT

We have studied the infrared properties of the brightest cluster galaxies (BCGs) located in the cores of X-ray-luminous clusters at $0.15 < z < 0.35$. The majority of the BCGs are not particularly infrared-luminous compared with other massive early-type galaxies, suggesting that the cluster environment has little influence on the infrared luminosities of the BCGs. The exceptions, however, are the BCGs in the three X-ray-brightest clusters in the sample, A1835, Z3146, and A2390. These BCGs have a prominent far-infrared peak in their spectral energy distributions (SEDs), and two of them (those in A1835 and Z3146) can be classified as luminous infrared galaxies (LIRGs: $L_{\rm IR} > 10^{11}\ L_{\odot}$). Although radio AGNs (active galactic nuclei) are found to be prevalent among the BCGs, the infrared luminosities of these three BCGs, judged from the infrared SED signatures, are likely to be powered by star formation. Considering the overall trend that clusters with shorter radiative gas cooling times harbor more infrared-luminous BCGs, the enhanced star formation may be caused by the cooling cluster gas accreting onto the BCGs.

Subject headings: cooling flows — galaxies: active — galaxies: clusters: general — galaxies: elliptical and lenticular, cD — infrared: galaxies

1. INTRODUCTION

Clusters of galaxies are embedded in a halo of diffuse hot gas ($T_{\rm gas} \sim 10^7$–10^8 K), which emits strongly in the X-ray through thermal bremsstrahlung radiation. The radiative cooling time of this hot intracluster plasma is usually comparable to the Hubble time, suggesting that the gas does not cool substantially over the age of the clusters. There are, however, clusters that show a highly peaked X-ray surface brightness profile in the core, which indicates that the hot gas in these cores is dense and has a substantially shorter cooling time. In extreme cases, the cooling time is estimated to be less than a few Gyr, which prompted the idea that these dense cores are sustaining an inflow of cooling gas toward the cluster center (Cowie & Binney 1977; Fabian & Nulsen 1977).

The reality of such a cluster "cooling flow" has been disputed over the years on the basis that the inferred gas cooling rate (which we assume to lead to a mass deposition rate) is simply too large to be consistent with the modest level of activity (e.g., Hα-derived star formation rates) seen in these cluster cores (see Fabian 1994 for a review of cooling flows). In the most extreme cases, the gas cooling rate was estimated to be >1000 $M_{\odot}$ yr^{-1} (e.g., Allen et al. 1996), and yet there is no sign of activity involving such a magnitude of mass inflow. Many of the brightest cluster galaxies (BCGs) in strongly cooling cores do show some signs of activity, such as visual emission lines and UV continuum (e.g., Allen 1995), but if they are due to star formation, the inferred star formation rate (e.g., from Hα) is only a few hundred $M_{\odot}$ yr^{-1} at most (e.g., Crawford et al. 1999). Considering that the BCGs in strongly cooling cores also show evidence for containing a significant amount of dust (Edge et al. 1999) and molecular gas (Edge 2001; Salomé & Combes 2003), it is clear that these BCGs are unusually active; what is puzzling, however, is the large difference between the gas cooling rate we infer and that we can account for.

A self-consistent picture is finally emerging from observations with *Chandra* and *XMM-Newton*. *XMM-Newton* especially has demonstrated convincingly for the first time that the cluster gas is cooling but not as much as originally thought. More specifically, *XMM-Newton* has detected strong emission from a cool plasma at temperatures half to one-third of the ambient value, but there is also a severe deficit of emission from plasma below these temperatures (Peterson et al. 2001, 2003; Tamura et al. 2001; Kaastra et al. 2001). In other words, there seems to be a floor of gas temperature below which cooling is no longer effective. The result is an order of magnitude reduction in the X-ray-derived mass deposition rates, making them consistent with the modest amount of activity observed at other wavelengths, such as the star formation rates derived from the extinction-corrected Hα emission (Crawford et al. 1999).

The current view is that some kind of gas heating (e.g., a radio jet from an AGN) slows the cooling process (see Begelman 2004 for a recent review). Indeed, such heating may play an important role in the process of galaxy formation in general because it would provide a way to suppress the formation of bright ($>L^*$) massive galaxies, which are overproduced in model calculations (Croton et al. 2006 and references therein). In fact, the BCGs in the cooling-flow clusters may prove to be an important laboratory

[1] Steward Observatory, University of Arizona, 933 North Cherry Avenue, Tucson, AZ 85721.
[2] Massachusetts Institute of Technology, Center for Space Research, Building 37, 70 Vassar Street, Cambridge, MA 02139-4307.
[3] OAMP, Laboratoire d'Astrophysique de Marseille, UMR6110 traverse du Siphon, 13012 Marseille, France.
[4] Division of Physics, Mathematics, and Astronomy, California Institute of Technology, 105-24, Pasadena, CA 91125.
[5] Associated with Observatoire de Paris, 92195 Meudon, France.
[6] School of Physics and Astronomy, University of Birmingham, Edgbaston, Birmingham, B15 2TT, England, UK.
[7] Institut d'Astrophysique Spatiale, bât 121, Université Paris Sud, F-91405 Orsay Cedex, France.
[8] *Spitzer* Science Center, California Institute of Technology 220-06, Pasadena, CA 91125.
[9] Harvard-Smithsonian Center for Astrophysics, 60 Garden Street, Mail stop 65, Cambridge, MA 02138.

where we can study the effects of cooling gas directly accreting onto a seed mass concentration, a condition that might be found in the first generation of forming galaxies at high redshift.

To investigate this cooling flow problem further, we have examined the *Spitzer* IRAC (3.6, 4.5, 5.8, and 8.0 μm) and MIPS (Multiband Imaging Photometer for *Spitzer*; 24, 70, and 160 μm) images of the BCGs located in the cores of X-ray-luminous clusters. At the redshifts of targeted clusters, IRAC detects stellar continuum light while MIPS detects thermal dust emission. Observations of emission from heated dust can detect deeply embedded forms of activity that are hidden from other search methods such as visual emission lines or UV continuum. For example, a galaxy with a star formation rate of $\sim$1000 $M_\odot$ yr^{-1} would be ultraluminous in the infrared ($L_{\rm IR} > 10^{12}$ $L_\odot$), so if any of the BCGs in the so-called cooling flow clusters are undergoing such vigorous star formation as a result of a massive gas inflow, they would stand out in the *Spitzer* mid/far-infrared images. The overall shape of spectral energy distribution (SED) will also tell us whether the infrared luminosity source is star formation or an AGN.

Throughout the paper we adopt the cosmological parameters of $\Omega_M = 0.3$, $\Omega_\Lambda = 0.7$, and $H_0 = 70$ km s^{-1} Mpc^{-1} except when noted otherwise.

2. THE SAMPLE

The 11 clusters for this study are listed in Table 1 and were part of a *Spitzer* GTO program described in Egami et al. (2006). The overall cluster selection criteria for this program are the following: (1) X-ray-luminous ($L_{\rm X} \gtrsim 5 \times 10^{44}$ ergs s^{-1} based on the published soft X-ray luminosities listed in Table 1), (2) moderate redshift ($z \sim 0.15$–0.5), and (3) low IR background ($N_{\rm H} < 3.5 \times 10^{22}$ cm^{-2}). We did not include clusters whose redshifts are based on a small number of measurements and those with severely limited ancillary data. Since the primary goal of this program is to study gravitationally lensed background galaxies, the most X-ray-luminous clusters were chosen under the assumption that they are the most massive clusters and therefore the most effective lenses. This means that these clusters were chosen without any regard to the properties of the BCGs. However, since, to a first order, the X-ray luminosity is proportional to the gas cooling rate, this cluster sample also provides a good data set to study the properties of BCGs in strongly cooling cluster cores.

The identification of the BCG in a cluster is usually straightforward. Many cluster cores harbor a single giant elliptical galaxy that dominates the brightness at the visual/near-infrared wavelengths and is located at/near the peak of the cluster X-ray emission. There are, however, cases in which a BCG cannot be identified uniquely: some clusters have more than one giant elliptical with similar brightnesses in the cluster core, or have a disturbed X-ray morphology without a well-defined peak. In these cases, it was not clear how we could relate the cluster gas properties (e.g., cooling rates) with those of the individual galaxies. For this study, we therefore chose only those clusters that show an X-ray morphology with a well-defined single peak and have a single 24 μm–detected BCG near the X-ray peak based on the archived *ROSAT* (*Röntgensatellit*) HRI images and on published *Chandra* images (e.g., Smith et al. 2005). We also note that based on the *Chandra* images, our sample contains both "relaxed" and "unrelaxed" clusters, and that the spatial coincidence of the X-ray peak and BCG is not precise in many of the "unrelaxed" clusters (e.g., Smith et al. 2005).

Table 1 lists the position of the BCG in each cluster as well as a few critical properties of these clusters such as X-ray luminosities and gas cooling times. Based on the classification by Allen & Fabian (1998), 7 out of the 11 clusters are classified as cooling flow clusters (CFs), while four are classified as non–cooling flow clusters (NCFs).

3. THE DATA

3.1. *Spitzer IRAC Data*

The 3.6, 4.5, 5.8, and 8.0 μm images were obtained using the Infrared Array Camera (IRAC; Fazio et al. 2004) on board the *Spitzer Space Telescope* (Werner et al. 2004). Each of the four IRAC channels uses a separate detector array. The 3.6 μm channel ($\lambda_c = 3.56$ μm, $\Delta\lambda = 0.75$ μm) and 4.5 μm channel ($\lambda_c = 4.52$ μm, $\Delta\lambda = 1.01$ μm) use 256×256 InSb arrays, while the 5.8 μm channel ($\lambda_c = 5.73$ μm, $\Delta\lambda = 1.42$ μm) and 8.0 μm channel ($\lambda_c = 7.91$ μm, $\Delta\lambda = 2.93$ μm) use 256×256 Si:As arrays. At any given time, two channels are used simultaneously (3.6 and 5.8 μm, or 4.5 and 8.0 μm). Each channel has a similar pixel size ($\sim$1.″2 pixel^{-1}) and field of view (5.′2 $\times$ 5.′2). Integration times were 2400 s per band except for A1835, whose integration times were 2400 s at 3.6 and 5.8 μm and 3600 s at 4.5 and 8.0 μm.[10] The images were taken with the small-step cycling dither pattern. The basic calibrated data (BCD) images were combined using a custom IDL mosaicking routine with the final pixel scale of 0.″6 pixel^{-1}, half of the instrument intrinsic pixel size.

The IRAC photometry used a circular beam with a diameter of 12.″2 with a sky background annulus of 6.″1–12.″2 in radius. We selected this rather large beam (6 times the point-spread function [PSF] FWHM) because at these wavelengths, some BCGs show a significant spatial extent. Although in some cases there is contamination from nearby sources falling into the beam, the effect is small because of the dominance of the BCGs. The point-source aperture corrections were applied, which were 1.061, 1.064, 1.067, and 1.089 at 3.6, 4.5, 5.8, and 8.0 μm, respectively, based on the IRAC Data Handbook.

The resultant 1 σ sensitivities in the mosaicked images are $\sim$5 μJy in all four bands. The shorter wavelength images do not necessarily go deeper when such a large photometry beam is used with IRAC images of this depth due to the confusion noise. A conservative estimate for the absolute calibration uncertainty is 10%.

3.2. *Spitzer MIPS Data*

The 24, 70, and 160 μm images were obtained using MIPS (Rieke et al. 2004). The MIPS 24 μm channel ($\lambda_c = 23.7$ μm, $\Delta\lambda = 4.7$ μm) uses a 128×128 BIB Si:As array with a pixel scale of 2.″55 pixel^{-1}. The 70 μm channel ($\lambda_c = 71.4$ μm, $\Delta\lambda = 19.0$ μm) uses a 16×32 Ge:Ga array with a pixel scale of 9.″98 pixel^{-1}. The 160 μm channel ($\lambda_c = 155.9$ μm, $\Delta\lambda = 35$ μm) uses a 2×20 stressed Ge:Ga array with a pixel scale of $16'' \times 18''$.

All the clusters in the sample (Table 1) were imaged at 24 μm using the large-source photometry mode. The total integration times were 3600 s pixel^{-1} at the position of the BCGs. Since we did not have enough observing time to observe all the BCGs at 70 and 160 μm, at these wavelengths we only observed the three BCGs brightest at 24 μm, for which we can expect a good chance of detection. For the two clusters with the brightest BCGs at 24 μm (A1835 and Z3146), we conducted 70 and 160 μm imaging using the large-source photometry mode. For the cluster with the third brightest BCG at 24 μm (A2390), we performed

[10] The IRAC data of A1835 were taken as part of the GTO program PID: 64 (PI: G. Fazio). All the other data were taken as part of the GTO program PID: 83 (PI: G. Rieke).

TABLE 1

TARGET CLUSTERS AND THEIR X-RAY PROPERTIES

				X-RAY LUMINOSITY				GAS COOLING TIME		
				ROSAT						
NAME[a]	R.A.[b] (J2000.0)	DECL.[b] (J2000.0)	z[c]	NORAS[d] (10^{44} ergs s^{-1})	BCS[e] (10^{44} ergs s^{-1})	*ASCA*[f] (10^{44} ergs s^{-1})	*Einstein* (EMSS)[g] (10^{44} ergs s^{-1})	*ROSAT*[h] (Gyr)	*Chandra*[i] (Gyr)	TYPE[j]
A773	09 17 53.4	+51 43 39	0.217	7.66	8.27	9.36	...	9.1	24.8	NCF
Z3146	10 23 39.6	+04 11 12	0.291	20.18	17.86	24.89	...	1.6	0.6	CF
MS 1358.1+6245	13 59 50.6	+62 31 05	0.327	6.14	...	7.51	7.38	2.7	...	CF
A1835	14 01 02.0	+02 52 45	0.252	21.24	25.14	29.68	...	1.4	0.6	CF
MS 1455.0+2232	14 57 15.1	+22 20 35	0.258	9.00	8.65	10.89	10.51	1.0	...	CF
A2218	16 35 49.3	+66 12 45	0.175	4.96	5.66	6.57	...	9.5	30.9	NCF
A2219	16 40 19.6	+46 42 43	0.228	15.54	13.03	24.84	...	8.4	29.1	NCF
A2261	17 22 27.2	+32 07 58	0.224	13.11	11.57	15.21	...	2.8	3.0	CF
MS 2137.3−2353	21 40 15.1	−23 39 39	0.313	...	...	11.68	10.73	1.1	...	CF
A2390	21 53 36.7	+17 41 45	0.233	16.13	...	26.49	...	3.9	1.9	CF
AC 114	22 58 48.4	−34 48 09	0.312	...	...	12.01	...	16.2	...	NCF

NOTES.—All the listed values correspond to the cosmological parameters (Ω_M, Ω_Λ, H_0 [km s^{-1} Mpc^{-1}]) of (0.3, 0.7, and 70). When converted from a different choice of the cosmological parameters, the X-ray luminosities were scaled with the inverse square of the luminosity distance. Since the gas temperature is independent of the choice of the cosmological parameters, the gas cooling time through bremsstrahlung emission scales with $n_e^{-1} \propto (Vp/L_X)^{1/2}$, where n_e, Vp, L_X are the electron density, proper volume, and luminosity of the X-ray-emitting gas. Units of right ascension are hours, minutes, and seconds, and units of declination are degrees, arcminutes, and arcseconds.

[a] The prefix "A" denotes the Abell clusters (Abell et al. 1989), while the prefix "MS" denotes the *Einstein* Extended Medium Sensitivity Survey clusters (Gioia & Luppino 1994). The Zwicky cluster Z3146 is often designated as ZwCl 1021.0+0426 (NED convention), while the cluster AC 114 is also known as the Abell supplementary southern cluster AS 1077 (Abell et al. 1989).

[b] These coordinates indicate the positions of the BCGs. The BCG position in MS 2137 was measured in the Palomar Digital Sky Survey image while other positions were taken from Smail et al. (2001) (A2218), Stanford et al. (2002) (MS 1358 and AC 114), and Crawford et al. (1999) (for the rest), respectively.

[c] All the redshifts were taken from Allen (2000).

[d] The 0.1–2.4 keV luminosity is from NORAS survey (Böhringer et al. 2000).

[e] The 0.1–2.4 keV luminosity is from BCS survey (Ebeling et al. 1998).

[f] The 2–10 keV luminosity is from *ASCA* (Allen 2000).

[g] 0.3–3.5 keV luminosity from the *Einstein* Medium Sensitivity Survey (Gioia & Luppino 1994).

[h] Radiative gas cooling times at the cluster center from Allen (2000) based on the *ROSAT* observations.

[i] Radiative gas cooling times at the cluster center from Bauer et al. (2005) based on the *Chandra* observations.

[j] Cooling flow (CF)/Non-cooling flow (NCF) classifications by Allen & Fabian (1998) (CF: 90%-conficence upper limit on $t_{cool} < 10$ Gyr). The *Chandra* cooling times by Bauer et al. (2005) do not affect the classification at least for these clusters.

only 70 μm imaging due to a high infrared sky background toward this direction. The integration times were 370 s pixel^{-1} at 70 μm, and 100 s pixel^{-1} at 160 μm at the position of the BCGs.

The data were reduced and combined with the Data Analysis Tool (DAT) developed by the MIPS instrument team (Gordon et al. 2005). A few additional processing steps were applied to the 24 μm data as well. First, special flat fields were constructed to remove artifacts in the flats produced by material deposited on the scan mirror. Second, the 24 μm array is subject to latent images after exposure to a bright source. The latent images manifest themselves as a region of reduced sensitivity centered on the array position of the bright source in subsequent exposures. These "dark latents" decay with time and disappear on the next anneal cycle. Several of our observations were contaminated by dark latents caused by bright 24 μm sources in the target fields. A source-free image of the latents was produced by median combining the entire data set with appropriate bright source masks. The dark latents were removed from each individual frame by dividing the frames by the normalized dark latent image prior to mosaicking. A detailed discussion of these instrumental effects will be presented in a forthcoming paper (G. H. Rieke et al. 2006, in preparation). A third processing step beyond the normal DAT processing was necessary owing to the design of the observations. Each cluster was observed using two Astronomical Observing Requests (AORs), and the two AORs were often separated by a significant amount of time. As a result, changing zodiacal backgrounds resulted in strong gradients in the resulting mosaics. To mitigate the effect of any DC offset between AORs, a mean row was subtracted from each individual data frame, again with an appropriate bright source mask, prior to mosaicking. The final mosaicked images were produced with pixel scales of 1.″25, 4.″92, and 8″ pixel^{-1} at 24, 70, and 160 μm, respectively, which are half of the instrument intrinsic pixel sizes.

The MIPS photometry beam diameters and corresponding inner/outer sky annulus radii are as follows: 26″ and 20″–32″ at 24 μm, 35″ and 39″–65″ at 70 μm, and 50″ and 75″–125″ at 160 μm. The point-source aperture corrections for these measurements are 1.167, 1.308, and 1.442, respectively, based on the MIPS instrument Web site. For the clusters A2218 and AC114, we used a smaller photometry beam (13.″2 diameter, aperture correction = 1.648) at 24 μm to prevent contamination from nearby sources. The 70 and 160 μm aperture corrections depend to some extent on the intrinsic color of the observed source, so we used the value for a red PSF ($T = 15$ K) at 70 μm and that for a blue PSF ($T = 1000$ K) at 160 μm, assuming that the infrared SEDs of the galaxies observed here are peaking somewhere between these two wavelengths. However, the effect of this color-dependent aperture correction is on the order of a few to several percent at most, well within the uncertainties of our photometric measurements.

The resultant 1 σ sensitivities in the mosaicked images are 0.01, 2.6, and 15 mJy at 24, 70, and 160 μm, respectively. The absolute calibration uncertainties are 10%, 20%, and 20% in these three bands.

3.3. *Chandra X-Ray Data*

For the three X-ray-brightest clusters in the sample (A1835, A2390, and Z3146), we have extracted all available data from the *Chandra* archive, and have reprocessed them to provide a uniform and consistent set of X-ray measurements. The initial *Chandra* results for A1835 have been published previously in Schmidt et al (2001). For A2390, an analysis of the combined 19 ks observation from Cycle 1 has been published in Allen et al. (2001); however, a subsequent deeper exposure was taken in Cycle 4, and we also included this data set. Finally, although observed during Cycle 1, the *Chandra* results for Z3146 remain unpublished. When all the data were combined, the total integration times for A1835, A2390, and Z3146 (after standard filtering) were 30 ks (with two data sets), 104 ks (with three data sets), and 46 ks (with one data set), respectively. The data processing and the method for calculating the gas cooling rates are described in the Appendix. Detailed analyses of the A2390 and Z3146 *Chandra* data will be published elsewhere (M. W. Wise 2006, in preparation).

3.4. *VLA* 1.4 GHz *Data*

We have compiled the 1.4 GHz flux densities of the BCGs from a number of sources. Where duplications exist, we have adopted the following priorities:

1. Deep high-resolution observations targeting clusters (Morrison et al. 2003; Rizza et al. 2003).
2. FIRST survey (Faint Images of the Radio Sky at Twenty cm, 2003 April 11 version; Becker et al. 1995; White et al. 1997).
3. NVSS survey (NRAO VLA Sky Survey; Condon et al. 1998).

The data published by Morrison et al. (2003) and Rizza et al. (2003) have the highest spatial resolution (1.″5, A configuration) and sensitivity ($\sigma \sim 25$–50 μJy). The FIRST and NVSS surveys have spatial resolutions of 5″ (B configuration) and 45″ (D configuration), and sensitivities of $\sigma \sim 140$ and 450 μJy, respectively. The flux densities from the NVSS should be used with caution because we see cases in which a single NVSS source at a BCG position breaks up into multiple radio components (e.g., Z3146) or is clearly displaced from the BCG (e.g., A2219) when observed with higher spatial resolution.

4. RESULTS

Figures 1 and 2 show the IRAC and MIPS images of the core regions of the 11 clusters. The measured *Spitzer* flux densities, as well as those at 1.4 GHz, are given in Table 2. When there is no radio detection (i.e., A773, A2218, and A2219), we list the 3 σ upper limit. Figure 1 shows the *Spitzer* images of the three BCGs that are the brightest at 24 μm. Figure 2 shows the rest of the sample. Note that these three BCGs are also the brightest in terms of the intrinsic mid-infrared luminosity since all the clusters studied here are at similar redshifts ($z \sim 0.2$–0.3). The SEDs produced from the IRAC/MIPS photometry are shown in Figure 3.[11]

The strong infrared sources in these three BCGs are compact, the 24 μm sources essentially being unresolved, which sets an upper limit on the source diameter (D) of $D < 20$ kpc for the size of the infrared emitting region. The BCGs are resolved at 8 μm with an estimated intrinsic size of $D \sim 8$ kpc, but the stellar light contribution (as opposed to thermal dust emission) may be significant at this wavelength. Therefore, we treat this size as an upper limit. This indicates that the infrared luminosity originates in the BCGs.

The rest of the BCGs in the sample show SEDs monotonically decreasing in the mid-infrared with no clear indication of having a significant amount of far-infrared luminosity. These SEDs could still peak in the far-infrared, but the corresponding far-infrared luminosities would be much smaller than those of the three infrared-bright BCGs. At the same time, all the BCGs are detected

[11] In this and subsequent figures in the paper, error bars are omitted when their sizes are comparable to or smaller than those of the plot symbols.

TABLE 2
Spitzer/VLA Flux Density Measurements of the BCGs

Name	3.6 μm (mJy)	4.5 μm (mJy)	5.8 μm (mJy)	8.0 μm (mJy)	24 μm (uJy)	70 μm (mJy)	160 μm (mJy)	1.4 GHz	
								mJy	Reference
A773.....	1.42	1.10	0.62	0.42	98 ± 14	...	...	<0.14[a]	1
Z3146.....	0.89	0.80	0.54	1.33	4099 ± 410	68 ± 14	157 ± 35	2.04	2
MS 1358	0.69	0.56	0.32	0.24	90 ± 13	...	...	2.61	2
A1835.....	2.17	2.03	1.42	5.14	17236 ± 1724	185 ± 37	305 ± 63	31.25	2
MS 1455	1.27	1.00	0.59	0.50	345 ± 37	...	...	5.62	2
A2218.....	1.18	0.86	0.52	0.31	84 ± 13	...	...	<0.14[a]	1
A2219.....	1.02	0.79	0.42	0.28	125 ± 15	...	...	<0.14[a]	3
A2261.....	2.15	1.66	0.90	0.65	347 ± 36	...	...	3.40	2
MS 2137	0.88	0.68	0.42	0.28	294 ± 31	...	...	3.8	4
A2390.....	1.08	0.87	0.53	0.67	1075 ± 108	8 ± 3	...	200	3
AC 114.....	0.95	0.79	0.48	0.30	160 ± 18	...	...	...	...

Notes.—All the BCGs are strongly detected in the IRAC bands, and therefore the IRAC photometric uncertainties are dominated by those of the absolute calibration. For the MIPS bands, the 1 σ error bars including both the measurement and calibration uncertainties are explicitly shown because the contribution from the former is not negligible for weak detections.

[a] 3 σ upper limit ($\sigma \sim 45$ μJy).

References.—(1) Morrison et al. (2003); (2) FIRST survey (Becker et al. 1995; White et al. 1997). The latest catalog (2003 April 11 version) is available from http://sundog.stsci.edu; (3) Rizza et al. (2003); (4) NVSS survey (Condon et al. 1998).

above 5 σ at 24 μm, indicating that these BCGs are not completely infrared-quiet.

Figure 3 also shows that none of the BCGs has a power-law SED in the infrared typical of an AGN-dominated galaxy. Instead, all of them show a gradual drop at $\lambda_{\rm rest} \sim 3$–$5$ μm, a characteristic of star-dominated SED (here, we see only the longer wavelength drop from the SED peak near 1.6 μm in the rest frame). In fact, despite the large variation in the mid/far-infrared range, the SEDs of the BCGs are quite similar at $\lambda_{\rm rest} \sim 3$–$5$ μm not only in terms of shape but also of luminosity. This indicates that the

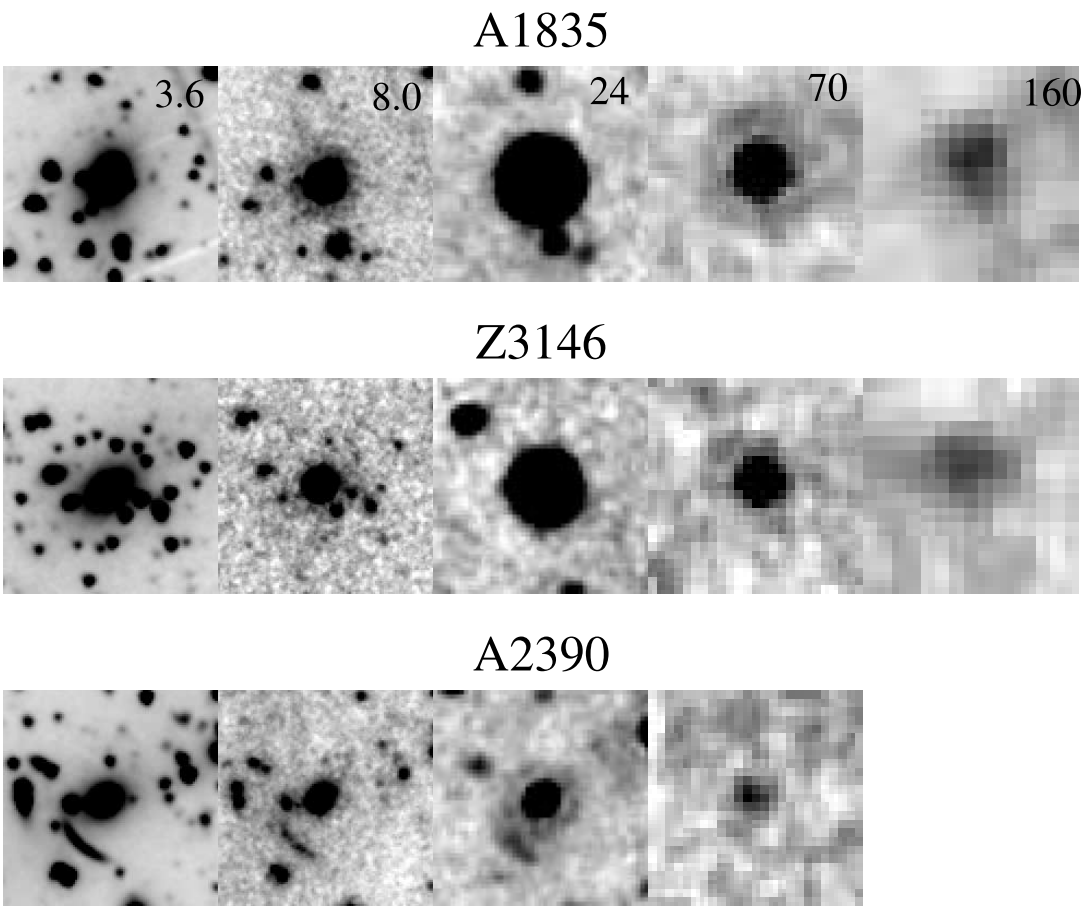

Fig. 1.—*Spitzer* images of the cluster cores harboring the three infrared-brightest BCGs. From left to right are the 3.6, 8.0, 24, 70, and 160 μm images, and the clusters are ordered vertically in decreasing 24 μm flux densities. North is up, and east is left. Each image is 1′ on a side, and the pixel scales are 0.″6 pixel^{-1} at 3.6 and 8.0 μm, 1.″25 pixel^{-1} at 24 μm, 4.″92 pixel^{-1} at 70 μm, and 8″ pixel^{-1} at 160 μm.

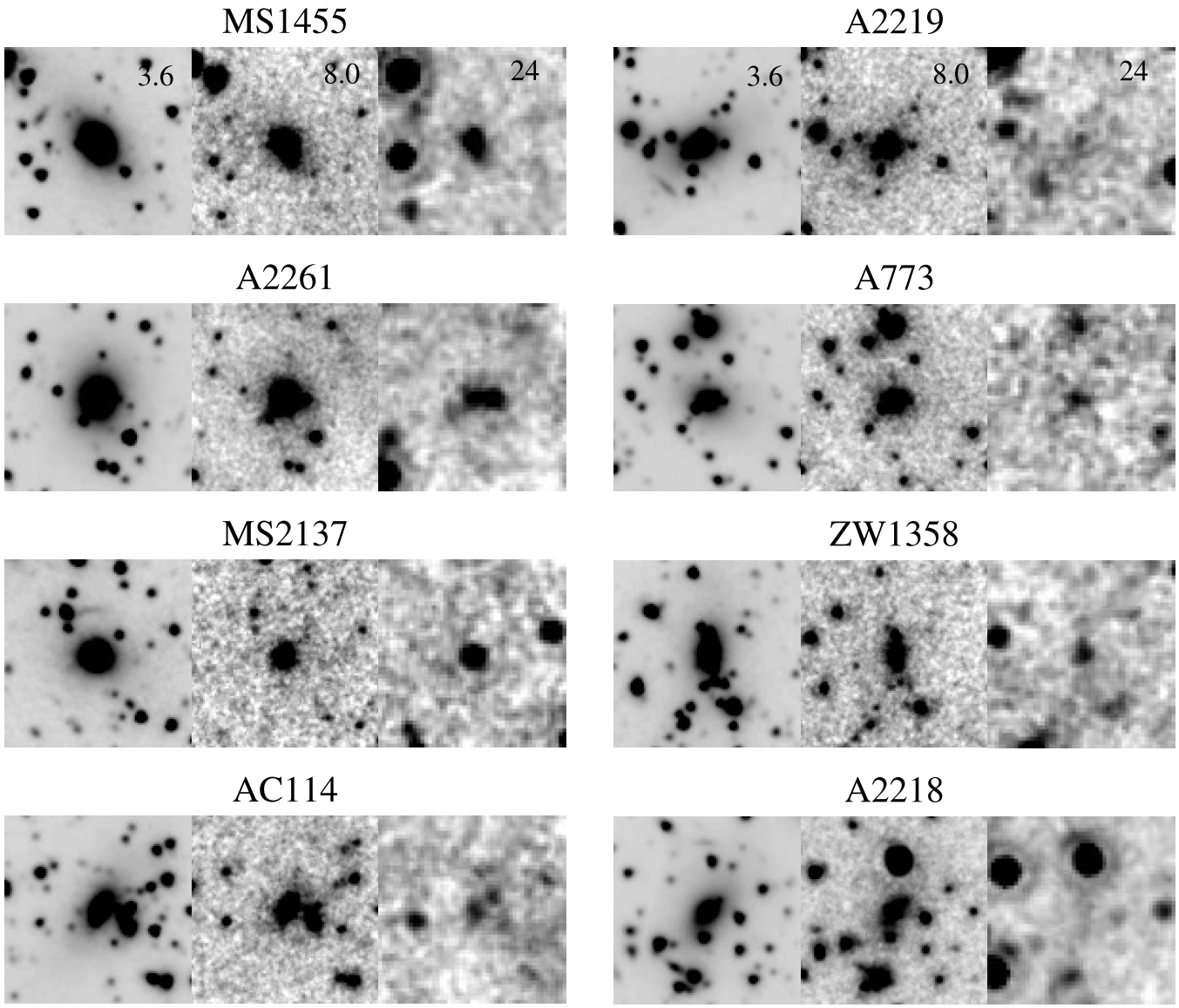

FIG. 2.—*Spitzer* images of the cluster cores for the rest of the sample. From left to right are the 3.6, 8, and 24 μm images, and the clusters are ordered vertically in decreasing 24 μm flux densities. North is up, and east is left. Each image is 1′ on a side, and the pixel scales are same as those in Fig. 1.

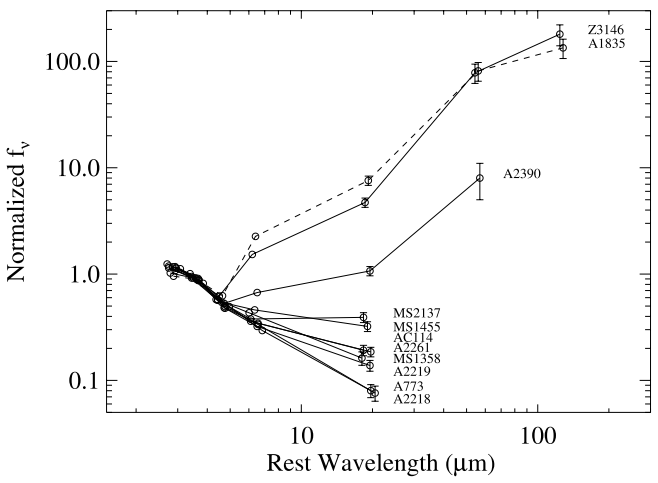

FIG. 3.—*Spitzer* SEDs of the BCGs. All the SEDs were scaled such that the flux densities coincide around 4.5 μm. The SED of the BCG in A1835 is denoted as a dashed line to make it distinguishable from that of Z3146.

near-infrared light of these BCGs is dominated by equally massive stellar populations, which are not directly related to the generation of the infrared luminosity.

5. DISCUSSION

5.1. *Infrared Properties of the BCGs*

Figure 4 plots the rest-frame 15 μm monochromatic luminosities of the BCGs against the soft X-ray (0.1–2.4 keV) luminosities of their parent clusters. The soft X-ray luminosity is a good measure of the intracluster gas cooling rate, and unlike the hard X-ray, it will not be affected severely by AGN emission. Table 1 lists the *ROSAT* soft X-ray (0.1–2.4 keV) luminosities from two *ROSAT* cluster catalogs, the *ROSAT* Brightest Cluster Sample (BCS; Ebeling et al. 1998) and the Northern *ROSAT* All-Sky (NORAS) Galaxy Cluster Survey (Böhringer et al. 2000). As seen in Table 1, the luminosities listed in these two catalogs are consistent with each other with a $\sim$10% uncertainty; we used the latter catalog by default. The two southern clusters, MS 2137.3−2353 and AC114, are not listed in the *ROSAT*-ESO Flux Limited X-Ray (REFLEX) Galaxy Cluster Survey (Böhringer et al.

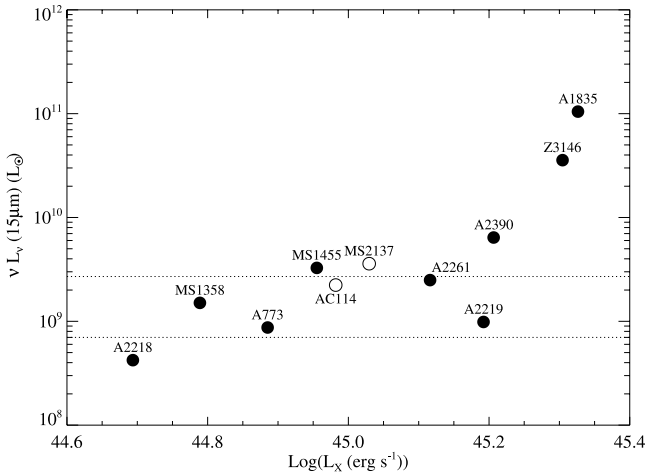

FIG. 4.—The 15 μm monochromatic luminosities (νL_ν) of the BCGs are plotted against the cluster soft X-ray (0.1–2.4 keV) luminosities from the NORAS survey (Böhringer et al. 2000). For the two southern clusters MS 2137 and AC 114 (*open circles*), we used the *Einstein* 0.3–3.5 keV (Gioia & Luppino 1994) and *ASCA* 2–10 keV (Allen 2000) X-ray luminosities, respectively. The latter was divided by a factor of 1.25 to account for the systematic offset between the *ROSAT* soft X-ray luminosities and *ASCA* hard X-ray luminosities. The horizontal dotted lines show the 1 σ range of the 15 μm monochromatic luminosities observed for local elliptical galaxies (Ferrari et al. 2002), which is $\nu L_\nu(15\ \mu\mathrm{m}) = (1.7 \pm 1) \times 10^9\ L_\odot$ (Note that these 15 μm luminosities are not those tabulated by Ferrari et al. [2002], which do not contain the stellar contribution, but those directly calculated from their flux density measurements.)

2004), the southern-sky version of NORAS, so instead we used the *Einstein* 0.3–3.5 keV (Gioia & Luppino 1994) and *ASCA* (*Advanced Satellite for Cosmology and Astrophysics*) 2–10 keV (Allen 2000) X-ray luminosities, respectively, as surrogates for the *ROSAT* soft X-ray luminosities. The latter needs to be divided by a factor of 1.25 to account for the systematic offset between the *ASCA* and *ROSAT* luminosities.[12]

We have estimated the rest-frame 15 μm monochromatic luminosities based on the SEDs shown in Figure 3. We chose to calculate the monochromatic luminosity at 15 μm because the conversion from the 15 μm luminosity to the total infrared luminosity is well established on the basis of *ISO* (*Infrared Space Observatory*) observations (Elbaz et al. 2002). For comparison, the 1 σ range of the 15 μm luminosities measured for local early-type galaxies by *ISO* (Ferrari et al. 2002) is shown (*horizontal dotted lines*). The figure shows that the majority of the BCGs studied here are not particularly luminous in the mid-infrared compared with the sample of Ferrari et al. (2002). Ferrari et al.'s sample may be biased toward infrared-active early-type galaxies, but this comparison at least shows that there is nothing special about the infrared luminosities of most BCGs, suggesting that the cluster environment has little influence on the BCG infrared properties in general.

The only exceptions are the BCGs in A1835, Z3146, and possibly A2390. The rest-frame 15 μm luminosities of the BCGs in A1835 and Z3146 are an order of magnitude or more larger than those of the rest of the sample. A2390 is an intermediate case in that its 15 μm luminosity is only slightly excessive

[12] Although the *ASCA* passband covers the hard X-ray and not soft X-ray, Table 1 shows that empirically there is a good scaling relation between the *ASCA* and *ROSAT* luminosities in the sense that the former is 1.25 ± 0.05 times larger than the latter when A2219 and A2390 are excluded. The hard X-ray luminosities of these two clusters are likely boosted by AGN emission. As we show later, the BCG in A2390 contains a strong radio AGN, while A2219 is known to have a strong radio source in the cluster core near the BCG.

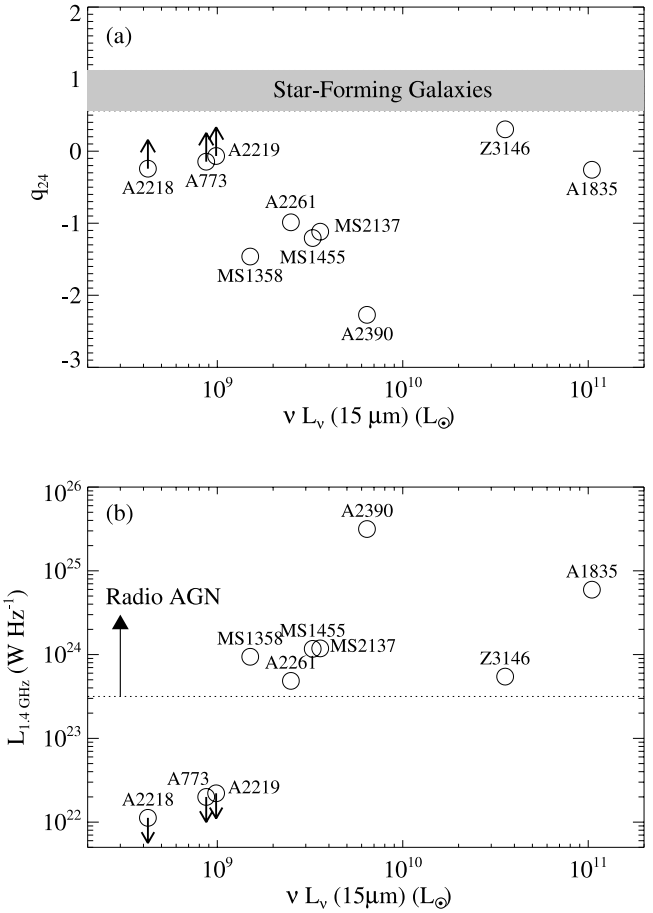

FIG. 5.—(*a*) The q_{24} parameter [$q_{24} = \log(S_{24\ \mu\mathrm{m}}/S_{20\ \mathrm{cm}})$] of the BCGs plotted against their 15 μm monochromatic luminosities. The shaded horizontal band shows the 1 σ range of the q_{24} parameter observed for the 24 μm–detected star-forming galaxies (Appleton et al. 2004). (*b*) The 1.4 GHz radio luminosities (L_ν) of the BCGs plotted against their 15 μm monochromatic luminosities. The radio luminosities were calculated as $L = 4\pi D_L^2 S_{1.4\ \mathrm{GHz}}$ (i.e., applying a *K*-correction assuming a radio continuum shape of $f_\nu \propto \nu^{-1}$.)

($\sim$5 σ), but the 70 μm photometry clearly shows that it has a prominent far-infrared peak in its SED.

These three infrared-brightest BCGs are located in the three most X-ray-luminous clusters in our sample, with soft X-ray (0.1–2.4 keV) luminosities of $(16\text{–}21) \times 10^{44}$ ergs s^{-1}. These three clusters also have short gas cooling times of 0.6–1.9 Gyr based on the latest *Chandra* results (Bauer et al. 2005) as shown in Table 1.

5.2. *Radio Emission*

Ten of the 11 BCGs (i.e., except for AC 114) have been observed in the radio (Table 2). Figure 5*a* plots the ratio of the flux densities at 24 μm and 20 cm parameterized as the q_{24} parameter [$q_{24} = \log(S_{24\ \mu\mathrm{m}}/S_{20\ \mathrm{cm}})$] (Appleton et al. 2004). The q_{24} values of star-forming galaxies fall in a well-defined range (0.84 ± 0.28) as a result of the radio-infrared luminosity correlation (Appleton et al. 2004), and therefore this parameter allows us to detect the existence of excess radio emission likely produced by a radio AGN. Figure 5*a* shows that seven of the 10 radio-observed BCGs are clearly out of the range for star-forming galaxies, having too much 20 cm radio flux density for their 24 μm flux density. The remaining three (those in A773, A2218, and A2219) are not detected in the radio with inconclusive lower limits on q_{24}.

Based on the 20 cm luminosities, this excessive radio emission in the BCGs is likely to originate from radio AGNs. Figure 5*b*

TABLE 3
PROPERTIES OF THE THREE INFRARED-BRIGHTEST BCGS

Parameter	A1835	Z3146	A2390
L_{IR} (10^{11} $L_\odot$)[a]	7.3 ± 1.5	4.1 ± 0.8	0.3 ± 0.1
SFR (IR) ($M_\odot$ yr^{-1})[b]	125 ± 25	70 ± 14	5 ± 1
L(Hα) (10^{40} ergs s^{-1})[c]	511 ± 105	594 ± 59	67 ± 18
SFR (Hα) ($M_\odot$ yr^{-1})[d]	40 ± 8	47 ± 5	5 ± 1
$S_{CO}\Delta V$ (J km s^{-1})[e]	7.7 ± 1.3	5.2 ± 1.2	...
L'_{CO} (10^{10} K km s^{-1} pc^2)[f]	2.4 ± 0.4	2.2 ± 0.5	...

NOTE.—For L_{IR} and SFR(IR) (i.e., the first two rows), we adopted a conservative uncertainty estimate of 20%, which corresponds to the absolute calibration uncertainties at 70 and 160 μm.

[a] Infrared luminosity calculated from the two-component modified blackbody SED models shown in Fig. 6.

[b] Star formation rate derived as $4.5\times10^{-44}L_{IR}$ (ergs s^{-1}) (Kennicutt 1998a).

[c] Extinction-corrected Hα luminosity from Crawford et al. (1999) rescaled with $\Omega_M = 0.3$, $\Omega_\Lambda = 0.7$, and $H_0 = 70$ km s^{-1} Mpc^{-1}.

[d] Star formation rate derived as $7.9\times10^{-42}L$(Hα)(ergs s^{-1}) (Kennicutt 1998a).

[e] Velocity-integrated line flux measured by Edge & Frayer (2003).

[f] CO (1–0) line luminosity calculated as $L'_{CO} = 3.25\times10^7 S_{CO}\Delta V \nu_{obs}^{-2} D_L^2 (1+z)^{-3}$, where $S_{CO}\Delta V$ is the velocity-integrated line flux in Jy km s^{-1}, ν_{obs} is observed frequency in GHz, and D_L is the luminosity distance in Mpc (Solomon et al. 1997).

shows that the 20 cm luminosities of these BCGs are mostly above $10^{23.5}$ W Hz^{-1}, which is usually the dividing line between AGNs and star-forming galaxies (e.g., Yun et al. 2001). All seven BCGs outside the range of star-forming galaxies in Figure 5*a* fall in the radio AGN category in Figure 5*b*. The prevalence of radio AGNs in the BCGs means that there may be a significant AGN contribution to the observed infrared luminosities of these galaxies.

The three BCGs with a low 20 cm luminosity ($\ll 10^{23.5}$ W Hz^{-1}), A773, A2218, and A2219, are all located in NCFs with a radiative gas cooling time of longer than 10 Gyr as categorized by Allen & Fabian (1998; see Table 1). They have the longest cooling times (24.8, 30.9, and 29.1 Gyr) of the 10 radio-observed clusters based on the latest estimates by Bauer et al. (2005; see Table 1). Such a trend is consistent with the earlier finding that there exists a strong coupling between cluster cooling cores and radio emission associated with the BCGs (e.g., Burns 1990), which may suggest that appreciable cooling of the intracluster gas in the cluster core tends to trigger a radio AGN in the BCG. The three clusters with no radio detection are also known to show bi/tri-modal dark matter distributions based on the lensing analysis by Smith et al. (2005). Such complex cluster mass distributions, together with the disturbed X-ray morphologies, may be related to the long gas cooling times.

5.3. *Properties of the Three Infrared-Brightest BCGs*

Here we examine in more detail the properties of the three infrared-brightest BCGs in the sample, those in A1835, Z3146, and A2390. Various properties of these three BCGs are summarized in Table 3.

Figure 6 shows the SEDs of the three BCGs. A number of photometric measurements in the literature are shown together with the *Spitzer* measurements. We modeled their behavior with a combination of the following three SED components: a giant elliptical (gE) SED, an infrared-luminous galaxy SED (Arp 220/M82), and a power-law radio spectrum simulating the radio emission from a radio AGN. The gE SED was taken from the SED template library of the Hyper-*z* photometric redshift code (Bolzonella et al. 2000). For infrared-luminous galaxy SEDs, we used those of Arp 220 and M82 taken from Silva et al. (1998). The SEDs of Silva et al. (1998) do not have the precision to reproduce individual spectral features (e.g., PAH features), but provide accurate broadband SEDs from ultraviolet to radio.

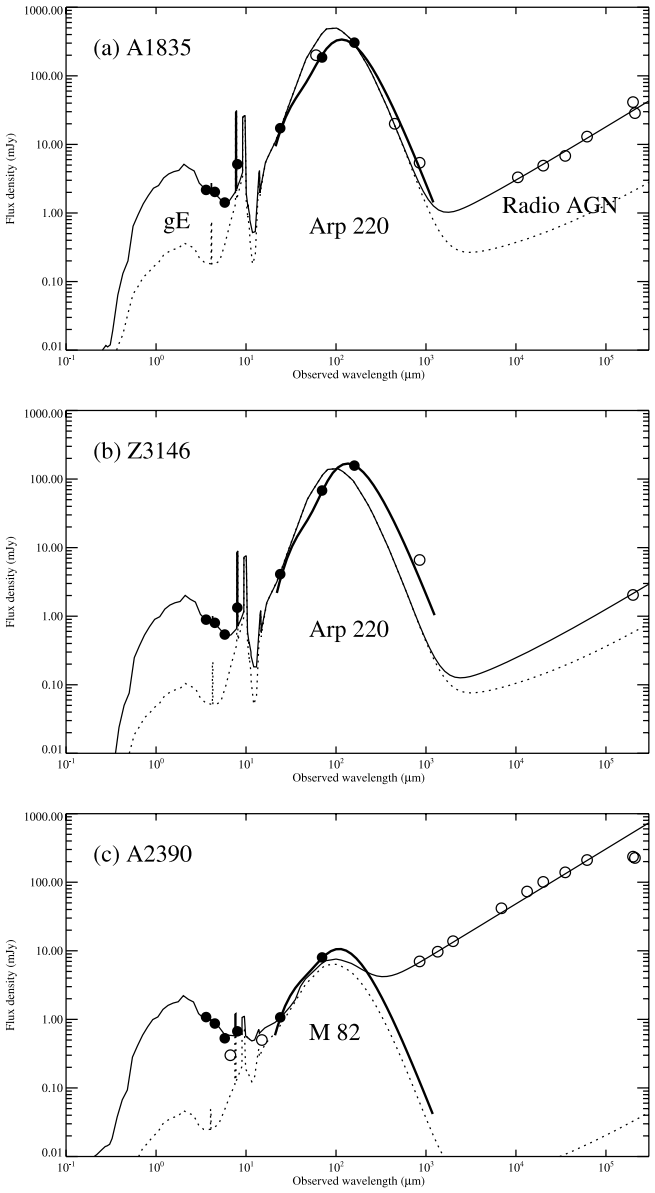

FIG. 6.—SEDs of the three infrared-brightest BCGs. The solid circles indicate the *Spitzer* measurements, while the open circles indicate the measurements in the literature (the error bars are comparable or smaller than the symbols). The dotted line shows the SEDs of (*a*, *b*) Arp 220 and (*c*) M82 (Silva et al. 1998). The thin solid line shows the three-component SED model, while the thick solid line shows the two-component modified blackbody SED model to fit the observed far-infrared/submillimeter SED (see the text for details). The flux density measurements of the BCGs in A1835 and A2390 were taken from Edge et al. (1999). The visual/near-infrared measurements were omitted because of the unknown aperture corrections, but they show a sharp drop toward shorter wavelengths typical of the SED of a giant elliptical. For A2390, we also excluded the low signal-to-noise *IRAS* measurements. The measurements for Z3146 were taken from Chapman et al. (2002; 850 μm) and the FIRST survey (20 cm).

The results are shown in Figure 6. As shown in Figure 6*a*, when the three components are combined, the gE SED dominates at $\lambda_{rest} \lesssim 5\mu$m, the radio AGN SED dominates at $\lambda_{rest} \gtrsim 1$ mm, and the infrared-luminous galaxy SED dominates between 5 μm and 1 mm. The scalings of the gE SED and radio AGN SED

were determined by the IRAC and radio measurements, respectively; the scaling of the infrared-luminous galaxy SED was set by the observed 24 μm flux density alone, and no effort was made to fit the far-infrared/submillimeter measurements. As shown in the figure, the BCGs in A1835 and Z3146 have a SED steeply rising from 24 to 70/160 μm, which requires an Arp 220-like SED to fit without violating the observed gE SED in the rest-frame visual/near-infrared. The BCG in A2390, on the other hand, has an SED significantly flatter between 24 and 70 μm, and in this case an M82-like SED is more appropriate.

Figure 6 shows that the three-component model works reasonably well to reproduce the observed SEDs of these three BCGs (*thin solid lines*). However, the figure also shows that the use of the template SEDs from a small number of well-known galaxies (Arp 220, M82) is clearly too simplistic, and does not work in detail. For example, the far-infrared SED peak at $\sim$100 μm seen with the BCGs in A1835 and Z3146 is clearly longward of that seen with Arp 220.

To determine the infrared luminosities of these BCGs accurately, we also fitted the far-infrared/submillimeter SEDs with a two-component modified blackbody model[13] (*thick solid lines*). These fits produced infrared luminosities of 7.3×10^{11}, 4.1×10^{11}, and 0.3×10^{11} $L_\odot$ for the BCGs in A1835, Z3146, and A2390, respectively. This also means that the BCGs in A1835 and Z3146 can be classified as LIRGs. Although Arp 220 is technically a ULIRG, its SED fits those of the BCGs in A1835 and Z3146 presumably because the infrared luminosity of Arp 220 (1.6×10^{12} $L_\odot$; Sanders et al. 2003) is barely above the ULIRG threshold. The infrared luminosity of the BCG in A2390 is also comparable to that of M82 (0.6×10^{11} $L_\odot$; Sanders et al. 2003).

The models in Figure 6 clearly show that the radio continuum flux is well above that expected from the Arp 220 SED. This is why these BCGs have small q_{24} values outside the range for star-forming galaxies (Fig. 5*a*), indicative of a radio AGN. However, the radio SEDs of the BCGs in both A1835 and A2390 show that the slope of the radio spectrum is steep ($\alpha \sim 0.8$, where $F_\nu \propto \nu^{-\alpha}$), and as a result the infrared luminosity is dominated by thermal dust emission in both BCGs, as found in general for steep spectrum radio galaxies (Shi et al. 2005). In the case of the BCG in Z3146, we do not have enough radio measurements to constrain the radio spectrum, but it is already clear from the SED in Figure 6 that it also has a large far-infrared peak.

Despite the presence of a radio AGN, all the BCGs show infrared SEDs typical of star-forming galaxies. In fact, none of the BCGs shows a power-law infrared SED typical of an AGN-dominated galaxy, and all of them show an excess of 8 μm emission, which is likely due to the 6.2 μm PAH feature in the passband at these redshifts. In the case of the BCG in Z3146, the existence of a strong 6.2 μm feature has been confirmed spectroscopically with a *Spitzer* IRS observation (E. Egami et al. 2006, in preparation), which indicates that star formation is a major contributor to the infrared luminosity.

A number of arguments indicate that the infrared luminosities are produced by star formation. From the infrared luminosities themselves, we derive star formation rates (SFRs) of 125, 70, and 5 $M_\odot$ yr^{-1} for the BCGs in A1835, Z3146, and A2390, respectively, using the relation of Kennicutt (1998a). Similar star formation rates are derived from the extinction-corrected Hα luminosities measured by Crawford et al. (1999) with the resultant values of 40, 47, and 5 $M_\odot$ yr^{-1} (Table 3). The Hα-derived star formation rates are often lower than those derived from the infrared luminosities (e.g., a factor of 3 lower with the BCG in A1835) probably due to the finite slit width (1.″2–1.″3) of the optical long-slit spectroscopy (Crawford et al. 1999). The infrared luminosities from the rest-frame 15 μm luminosities using the relation of Elbaz et al. (2002) for star-forming galaxies are 9.5×10^{11}, 3.3×10^{11}, and 0.6×10^{11} $L_\odot$, similar to the values directly measured above. Most recently, Hicks & Mushotzky (2005) showed that the BCGs in A1835 and Z3146 have a significant UV excess, which corresponds to the star formation rates of 123 ± 5 and 91 ± 4 $M_\odot$ yr^{-1}, respectively (Salpetev IMF). The excellent agreement between their estimates and ours not only supports the idea that these BCGs harbor strong star formation, but also implies that the amount of internal extinction is small.

One major difference between the SEDs of these BCGs and those of infrared-luminous galaxies is that the former are much more luminous in the rest-frame visual and near-infrared. At $\lambda_{\rm rest} < 5$ μm, the massive old stellar population in the BCGs completely overwhelms the light associated with the star-forming population. In fact, the total luminosity emitted in the visual/near-infrared from the massive old stellar population is comparable to that emitted by dust in the infrared. This explains why it has been difficult

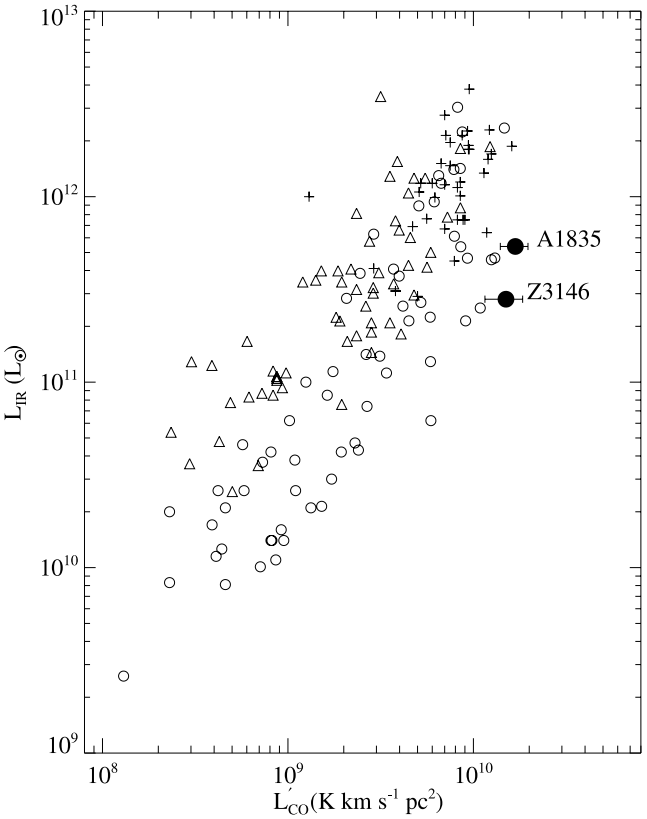

FIG. 7.—Infrared luminosity and CO (1–0) line luminosity of the BCGs in A1835 and Z3146 (*solid circles*) are compared with those of LIRGs and ULIRGs. See the notes of Table 3 for the definition of the CO line luminosity, $L'_{\rm CO}$. The LIRG/ULIRG points shown are from Sanders et al. (1991; *triangles*), Solomon et al. (1997; *crosses*), and Gao & Solomon (2004; *open circles*). The infrared luminosity and CO line luminosity of the two BCGs listed in Table 3 were rescaled to the values with $H_0 = 75$ km s^{-1} Mpc^{-1} and $q_0 = 0.5$ so that the direct comparison with the LIRG/ULIRG sample is possible.

[13] Each modified blackbody model was represented by the following analytical expression: $F_\nu = B_\nu(T_d)(1 - e^{-(\nu/\nu_0)^\beta})$, where $B_\nu(T_d)$ is the Planck function with a dust temperature T_d, ν_0 is the frequency below which the thermal dust emission becomes optically thin, and β is the dust emissivity power-law index. A good fit was obtained for the BCG in A1835 with $T_d = 40$ and 110 K, $\nu_0 = 3$ THz (i.e., 100 μm), and $\beta = 1.5$. The same dust temperatures were adopted for the BCG in A2390, which does not have any far-infrared/submillimeter measurements to constrain the SED, while dust temperatures of 35 and 100 K were used for the BCG in Z3146.

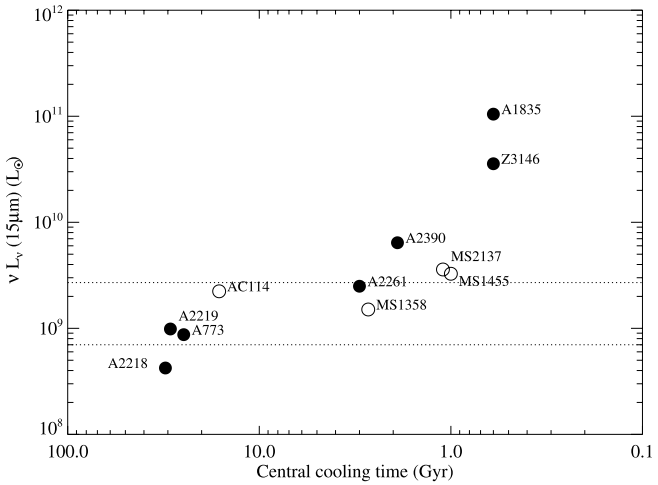

FIG. 8.—The 15 μm monochromatic luminosities of the BCGs plotted against the radiative cooling times of cluster gas derived from *Chandra* observations by Bauer et al. (2005; *solid circles*) and from *ROSAT* observations by Allen (2000; *open circles*). The horizontal dotted lines show the 1 σ range of the 15 μm monochromatic luminosities observed for local ellipticals shown in Fig. 4.

to detect the starbursting component in these BCGs. A similar object (i.e., a giant elliptical containing a starbursting population) has also been found in the field by Krause et al. (2003).

The two infrared-brightest BCGs, those in A1835 and Z3146, show another interesting property: exceptional strength of the CO (1–0) emission line for their infrared luminosities. Figure 7 shows a broad correlation that holds between the infrared luminosities and CO luminosities of LIRGs and ULIRGs. Plotted in the same figure, the BCGs in A1835 and Z3146 hint at the possibility that they are overluminous in CO luminosity when compared with LIRGs and ULIRGs with similar infrared luminosities. This may mean that these two BCGs contain an unusually large amount of cold molecular gas.

5.4. *Implications for the Cluster Cooling Flows*

Figure 8 plots the 15 μm monochromatic luminosities of the BCGs as a function of the radiative cooling time of the intracluster gas calculated by Bauer et al. (2005). Over the whole sample, there seems to be a trend that BCGs in clusters with shorter gas cooling times (and therefore larger X-ray luminosities in general) have larger infrared luminosities. Such a correlation would indicate that the infrared activity of a single galaxy at the cluster center is somehow connected to the property of a cluster core as a whole.

Note, however, that a large X-ray luminosity does not always translate into a short cooling time. For example, A2219 has a large X-ray luminosity but a long cooling time. In fact, A2219 is a peculiar cluster in that it highly deviates from the cluster X-ray luminosity-temperature (L_X vs. T) relation and mass-temperature (M vs. T) relation (Smith et al. 2005). This cluster may have experienced a core-penetrating merger recently (Smail et al. 1995), and such a process might have boosted the X-ray temperature and luminosity (Smith et al. 2005). In any case, the fact that A2219 deviates from the overall trend in Figure 4 but not in Figure 8 suggests that the correlation between the 15 μm luminosity and gas cooling time is more fundamental than that between the 15 μm luminosity and X-ray luminosity.

In general, the increased infrared luminosities observed in local galaxies are thought to be episodic. For example, transient galaxy-galaxy interactions are believed to boost the infrared luminosity by triggering vigorous star-formation and/or fueling an AGN. However, the process that triggered the increased infrared activity in the BCGs in A1835, Z3146, and A2390 is difficult to explain in terms of similar processes since in this case the infrared luminosity of a BCG would likely increase independent of the properties of the cluster in which it resides. In other words, in this scenario there is nothing that would prevent a BCG in a low X-ray luminosity and long cooling time cluster from becoming infrared-luminous. This would introduce a significant scatter in the correlations of the BCG mid-infrared luminosity with the cluster X-ray luminosity (Fig. 4) and with the cluster radiative gas cooling time (Fig. 8). The fact that we do not see significantly deviant points from these trends suggests that the triggering mechanism is not a stochastic process but rather a process that is controlled by the properties of the cluster cores as a whole.

An attractive possibility is to associate the observed infrared luminosity with the fate of the cooling cluster gas. In this case, only those BCGs in clusters with a short gas cooling time could become infrared-luminous because only these clusters could channel the gas into the BCGs and form stars. This hypothesis can be tested by comparing the infrared-derived SFRs with the X-ray-derived mass deposition rates.

Table 4 lists various determinations of the mass deposition rates for A1835, Z3146, and A2390 based on the X-ray spectral analysis. Together with the previously published values, we also list our own estimates based on the reanalysis of the *Chandra*

TABLE 4
MASS DEPOSITION RATES FOR THE THREE X-RAY-BRIGHTEST CLUSTERS

	Chandra					*XMM-Newton*
CLUSTER	Schmidt et al. (2001)[a] (<24 kpc)	Allen et al. (2001)[a] (<40 kpc)	This Work[b] (<50 kpc)	Voigt & Fabian (2004)[c] (<100 kpc)	This Work[d] (<500–700 kpc)	(Peterson et al. 2001) (<120 kpc)
A1835.....	130–200	...	<20	34^{+43}_{-34}	100^{+100}_{-70}	<130
Z3146.....	...	...	290^{+100}_{-100}	...	670^{+160}_{-170}	...
A2390.....	...	130–190	110^{+40}_{-30}	339^{+42}_{-118}	420^{+90}_{-80}	...

NOTES.—All the numbers are in units of $M_\odot$ yr^{-1}, and the error bars indicate the 90% confidence limits. The numbers in the parentheses indicate the radius of the region inside which the mass deposition rate was calculated. The mass deposition rate scales with the inverse square of the luminosity distance, and all the published values have been rescaled with $\Omega_M = 0.3$, $\Omega_\Lambda = 0.7$, and $H_0 = 70$ km s^{-1} Mpc^{-1}. The *XMM*-derived mass deposition rate for A1835 by Peterson et al. (2001) was rescaled with a luminosity distance of 1272 Mpc.

[a] We adopted the mass deposition rate of 200–300 $M_\odot$ yr^{-1} at $r < 30$ kpc for A1835 and at $r < 50$ kpc for A2390 ($\Omega_M = 1$, $\Omega_\Lambda = 0$, and $H_0 = 50$ km s^{-1} Mpc^{-1}).

[b] The centeral mass deposition rates derived for the $r < 13''$ region, which is the size of the 24 μm photometry beam. This radius corresponds to 51, 57, and 48 kpc at the distances of A1835, Z3146, and A2390, respectively.

[c] The deposition rates were calculated inside the region where the gas cooling time is less then 5 Gyr. This roughly corresponds to 100 kpc for A1835 and A2390.

[d] The total mass deposition rates calculated within the maximum radii of 490, 460, and 700 kpc at the distances of A1835, A2390, and Zw 3146, respectrively.

data. We calculated the mass deposition rates at the cluster center within a radius of 13″ (~50 kpc) from the BCGs (i.e., the size of the 24 μm photometry beam) as well as for the entire clusters ($r < 500-700$ kpc). The central mass deposition rates are more relevant for comparison with the star formation rates in the BCGs, and can be compared with other published *Chandra*-derived mass deposition rates, which were also calculated within comparable radii (Table 4). We did not list the mass deposition rates derived from the *ROSAT* and *ASCA* data because they are believed to be overestimated by almost an order of magnitude in many cases. The large mass deposition rates resulting from the *ROSAT* and *ASCA* data, exceeding 1000 $M_{\odot}$ yr^{-1} in extreme cases, are thought to originate from the existence of cool ambient gas in the cluster core, which, when spatially unresolved, tends to be included into the cooling-flow calculation and inflates the mass deposition rates (Allen et al. 2001). The difference between the central ($r < 50$ kpc) and total ($r < 500-700$ kpc) mass deposition rates listed in Table 4 reflects the size of this effect.

Table 4 shows that the various estimates of the mass depostion rates are not always consistent. In the case of A1835, for example, the value of 130–200 $M_{\odot}$ yr^{-1} ($r < 24$ kpc) derived by Schmidt et al. (2001) is significantly larger than the other estimates. In fact, Voigt & Fabian (2004) point out that the existing *Chandra* data of A1835 at $r < 100$ kpc is statistically consistent with the absence of the cooling-flow component, and our reanalysis of the same data is in line with this result. In the case of A2390, the various estimates are broadly consistent with each other, especially if we account for the effect mentioned above, which would inflate the mass deposition rate as we increase the region to extract the X-ray spectrum. In the case of Z3146, we do not have any other estimates to compare at this point, but this cluster provides the most convincing evidence for having a significant mass deposition rate. The differences between the various estimates probably reflect the level of uncertainty inherent in such analyses, and some part of the differences may be attributed to the improvements in the *Chandra* ACIS calibration since the early years of the mission.

The infrared-derived SFRs for the BCGs in A1835, Z3146, and A2390 are 125, 70, and 5 $M_{\odot}$ yr^{-1}, respectively, while the X-ray-derived mass deposition rates at the cluster center are <20, 290, and 110 $M_{\odot}$ yr^{-1}, respectively, based on our own estimates. This indicates that the correspondence between the infrared-derived SFRs and X-ray-derived mass deposition rates is currently suggestive at best. Z3146 is the only case where the two quantities are broadly consistent (within a factor of several). A2390 shows a large difference (a factor of 20), which may be related to the strong radio AGN detected in the BCG of this cluster. In the case of A1835, the difference seems at least a factor of 6 although we are in need of deeper *Chandra* data to better constrain the mass deposition rate and reconcile the conflicting estimates for the mass deposition rate.

Given the complex nature of star formation processes and the limited accuracy with the determination of the physical quantities such as star formation rates and mass deposition rates, it would not be surprising that the infrared-derived SFRs and X-ray-derived mass deposition rates differ by a factor of several or more even if there is a causal connection between the two. For example, the well-known Schmidt law (i.e., the correlation between the surface densities of gas and star formation rate seen in external galaxies) has a 1 σ scatter of a factor of 2, and individual galaxies deviate by as much as a factor of 7 (Kennicutt 1998b). Therefore, at least in Z3146 (and possibly in A1835), it is possible to interpret the observed SFRs as a result of the cooling cluster gas accreting onto the BCGs and triggering star formation (i.e., the cooling-flow interpretation). Such a scenario is also consistent with the exceptionally strong CO line emission observed with these two BCGs since cold molecular gas is seen to be accreting to the BCG in one of the low-redshift cooling-flow clusters (Salomé & Combes 2004).

6. CONCLUSIONS

With the *Spitzer* IRAC (3.6–8.0 μm) and *Spitzer* MIPS (24–160 μm) imaging data, we studied the infrared properties of the brightest cluster galaxies (BCGs) located in the cores of X-ray-luminous clusters. The main results are as follows:

1. The majority of BCGs are not infrared-luminous. Out of the 11 BCGs studied here, only three (those in A1835, Z3146, and A2390) have a strong far-infrared SED peak, and only two (those in A1835 and Z3146) can be classified as LIRGs (>10^{11} $L_{\odot}$).
2. There seems to be a trend that clusters with larger X-ray luminosities and shorter gas cooling times harbor more infrared-luminous BCGs. The three infrared-brightest BCGs (those in A1835, Z3146, and A2390) were found in clusters with the largest X-ray luminosities and shortest radiative gas cooling times in the sample.
3. The infrared luminosities of the three infrared-brightest BCGs are likely to be powered by star formation, judging from the infrared SED signatures. The infrared-derived SFRs are comparable to the extinction-corrected Hα-derived SFRs.
4. Radio AGNs are prevalent in the BCGs. Seven out of the 10 radio-observed BCGs studied here contain a luminous radio source (>$10^{23.5}$ W Hz^{-1} at 20 cm) and show a low 24 μm/20 cm flux density ratio, both indicative of a radio AGN.
5. The infrared-derived SFR of the BCG and the X-ray-derived mass deposition rate in the parent cluster are broadly consistent in Z3146 (and possibly in A1835), suggesting the interpretation that the observed star formation is triggered by the cooling cluster gas accreting onto the BCGs except when there is a strong radio AGN, as is the case in A2390.

This work is based on observations made with the *Spitzer* Space Telescope, which is operated by the Jet Propulsion Laboratory, California Institute of Technology under a contract with NASA (contract 1407). Support for this work was provided by NASA through an award issued by JPL/Caltech (contracts 960785 and 1255094). G. P. S. acknowledges financial support from Caltech and a Royal Society University Research Fellowship.

REANALYSIS OF THE *CHANDRA* X-RAY DATA

The *Chandra* data were reanalyzed using CIAO 3.2 and the latest calibration files available in CALDB 3.1. Each individual data set was reprocessed and screened to remove periods of strong background flares in the standard manner. Matching background event files were created for each data set from the standard ACIS blank-sky event files following the procedure described in Vikhlinin et al. (2005).

For a given cluster, we have calculated the total gas cooling rate for the entire cluster as well as the cooling rate in the immediate surrounding of the BCG (within a radius of 13″, which is the size of the 24 μm photometry beam). The total cooling rates were calculated

based on fits to the integrated spectrum inside a maximum outer radius. In practice, this radius was determined from the radial surface brightness and defined as the point at which the surface brightness profile drops below the background level. For A1835 and A2390, the individual data sets were combined to form a mosaic and the radial surface brightness determined for this composite. With this definition, the corresponding maximum radii are 125″ (∼490 kpc), 125″ (∼460 kpc), and 160″ (∼700 kpc) for A1835, A2390, and Z3146, respectively.

To calculate the gas cooling rates, spectra in a given region were extracted in the 0.5–7.0 keV energy range along with corresponding background spectra from the blank-sky event files mentioned previously. Counts weighted detector response files (RMFs) and effective area files (ARFs) were created for the extraction regions using the CIAO tools `mkacisrmf` and `mkwarf`. The resulting spectra were then compared to various standard spectral models using the XSPEC model library available in the ISIS spectral fitting package (Houck & Denicola 2000). The fitted spectral model was defined to consist of foreground Galactic absorption, a single-temperature thermal plasma (MEKAL) due to emission from the hot, outer cluster, and an isobaric cooling flow component (MKCFLOW). Fits were performed with the Galactic column fixed to the standard value as well as allowing it to varying. For the two clusters with multiple observations, individual spectra were extracted for each data set and the model was fit to the component spectra simultaneously. For A1835 and Z3146, the fits with and without varying Galactic columns gave comparable χ^2 values and the cooling rates quoted in Table 4 are for the fixed column fits. Fits for A2390 showed a marked improvement in χ^2 if the Galactic column was increased by ∼30% and the result from this fit is quoted in Table 4.

REFERENCES

Abell, G. O., Corwin, H. G., & Olowin, R. P. 1989, ApJS, 70, 1
Allen, S. W. 1995, MNRAS, 276, 947
———. 2000, MNRAS, 315, 269
Allen, S. W., Ettori, S., & Fabian, A. C. 2001, MNRAS, 324, 877
Allen, S. W., & Fabian, A. C. 1998, MNRAS, 297, L63
Allen, S. W., Fabian, A. C., Edge, A. C., Bautz, M. W., Furuzawa, A., & Tawara, Y. 1996, MNRAS, 283, 263
Appleton, P. N., et al. 2004, ApJS, 154, 147
Bauer, F. E., Fabian, A. C., Sanders, J. S., Allen, S. W., & Johnstone, R. M. 2005, MNRAS, 359, 1481
Becker, R. H., White, R. L., & Helfand, D. J. 1995, ApJ, 450, 559
Begelman, M. C. 2004, in Coevolution of Black Holes and Galaxies, ed. L. C. Ho (Cambridge: Cambridge Univ. Press), 374
Böhringer, H., et al. 2000, ApJS, 129, 435
———. 2004, A&A, 425, 367
Bolzonella, M., Miralles, J.-M., & Pelló, R. 2000, A&A, 363, 476
Burns, J. O. 1990, AJ, 99, 14
Chapman, S. C., Scott, D., Borys, C., & Fahlman, G. G. 2002, MNRAS, 330, 92
Condon, J. J., Cotton, W. D., Greisen, E. W., Yin, Q. F., Perley, R. A., Taylor, G. B., & Broderick, J. J. 1998, AJ, 115, 1693
Cowie, L. L., & Binney, J. 1977, ApJ, 215, 723
Crawford, C. S., Allen, S. W., Ebeling, H., Edge, A. C., & Fabian, A. C. 1999, MNRAS, 306, 857
Croton, D. J., et al. 2006, MNRAS, 365, 11
Ebeling, H., Edge, A. C., Bohringer, H., Allen, S. W., Crawford, C. S., Fabian, A. C., Voges, W., & Huchra, J. P. 1998, MNRAS, 301, 881
Edge, A. C. 2001, MNRAS, 328, 762
Edge, A. C., & Frayer, D. T. 2003, ApJ, 594, L13
Edge, A. C., Ivison, R. J., Smail, I., Blain, A. W., & Kneib, J.-P. 1999, MNRAS, 306, 599
Egami, E., et al. 2006, in ASP Conf. Ser., The *Spitzer* Space Telescope: New Views of the Cosmos, ed. L. Armus (San Francisco: ASP), in press (astro-ph/0603657)
Elbaz, D., Cesarsky, C. J., Chanial, P., Aussel, H., Franceschini, A., Fadda, D., & Chary, R. R. 2002, A&A, 384, 848
Fabian, A. C. 1994, ARA&A, 32, 277
Fabian, A. C., & Nulsen, P. E. J. 1977, MNRAS, 180, 479
Fazio, G. G., et al. 2004, ApJS, 154, 10
Ferrari, F., Pastoriza, M. G., Macchetto, F. D., Bonatto, C., Panagia, N., & Sparks, W. B. 2002, A&A, 389, 355
Gao, Y., & Solomon, P. M. 2004, ApJS, 152, 63
Gioia, I. M., & Luppino, G. A. 1994, ApJS, 94, 583
Gordon, K. D., et al. 2005, PASP, 117, 503
Hicks, A. K., & Mushotzky, R. 2005, ApJ, 635, L9
Houck, J. C., & Denicola, L. A. 2000, in ASP Conf. Ser. 216, Astronomical Data Analysis Software and Systems IX, ed. N. Manset, C. Veillet, & D. Crabtree (San Francisco: ASP), 591
Kaastra, J. S., Ferrigno, C., Tamura, T., Paerels, F. B. S., Peterson, J. R., & Mittaz, J. P. D. 2001, A&A, 365, L99
Kennicutt, R. C. 1998a, ARA&A, 36, 189
———. 1998b, ApJ, 498, 541
Krause, O., Lisenfeld, U., Lemke, D., Haas, M., Klaas, U., & Stickel, M. 2003, A&A, 402, L1
Morrison, G. E., Owen, F. N., Ledlow, M. J., Keel, W. C., Hill, J. M., Voges, W., & Herter, T. 2003, ApJS, 146, 267
Peterson, J. R., Kahn, S. M., Paerels, F. B. S., Kaastra, J. S., Tamura, T., Bleeker, J. A. M., Ferrigno, C., & Jernigan, J. G. 2003, ApJ, 590, 207
Peterson, J. R., et al. 2001, A&A, 365, L104
Rieke, G. H., et al. 2004, ApJS, 154, 25
Rizza, E., Morrison, G. E., Owen, F. N., Ledlow, M. J., Burns, J. O., & Hill, J. 2003, AJ, 126, 119
Salomé, P., & Combes, F. 2003, A&A, 412, 657
———. 2004, A&A, 415, L1
Sanders, D. B., Mazzarella, J. M., Kim, D.-C., Surace, J. A., & Soifer, B. T. 2003, AJ, 126, 1607
Sanders, D. B., Scoville, N. Z., & Soifer, B. T. 1991, ApJ, 370, 158
Schmidt, R. W., Allen, S. W., & Fabian, A. C. 2001, MNRAS, 327, 1057
Shi, Y., et al. 2005, ApJ, 629, 88
Silva, L., Granato, G. L., Bressan, A., & Danese, L. 1998, ApJ, 509, 103
Smail, I., Hogg, D. W., Blandford, R., Cohen, J. G., Edge, A. C., & Djorgovski, S. G. 1995, MNRAS, 277, 1
Smail, I., Kuntschner, H., Kodama, T., Smith, G. P., Packham, C., Fruchter, A. S., & Hook, R. N. 2001, MNRAS, 323, 839
Smith, G. P., Kneib, J.-P., Smail, I., Mazzotta, P., Ebeling, H., & Czoske, O. 2005, MNRAS, 359, 417
Solomon, P. M., Downes, D., Radford, S. J. E., & Barrett, J. W. 1997, ApJ, 478, 144
Stanford, S. A., Eisenhardt, P. R., Dickinson, M., Holden, B. P., & De Propris, R. 2002, ApJS, 142, 153
Tamura, T., et al. 2001, A&A, 365, L87
Vikhlinin, A., Markevitch, M., Murray, S. S., Jones, C., Forman, W., & Van Speybroeck, L. 2005, ApJ, 628, 655
Voigt, L. M., & Fabian, A. C. 2004, MNRAS, 347, 1130
Werner, M. W., et al. 2004, ApJS, 154, 1
White, R. L., Becker, R. H., Helfand, D. J., & Gregg, M. D. 1997, ApJ, 475, 479
Yun, M. S., Reddy, N. A., & Condon, J. J. 2001, ApJ, 554, 803